

# Temperature-dependent Raman spectroscopy, domain morphology and photoluminescence studies in lead-free BCZT ceramic

Indrani Coondoo<sup>a,\*</sup>, Neeraj Panwar<sup>b</sup>, Svetlana Krylova<sup>c</sup>, Alexander Krylov<sup>c</sup>, Denis Alikin<sup>a,d</sup>, Suresh Kumar Jakka<sup>e</sup>, Anton Turygin<sup>d</sup>, Vladimir Ya. Shur<sup>d</sup>, Andrei L. Kholkin<sup>a</sup>

<sup>a</sup> Department of Physics & CICECO – Aveiro Institute of Materials, University of Aveiro, 3810-193, Aveiro, Portugal

<sup>b</sup> Department of Physics, Central University of Rajasthan, Bandarsindri, 305817, Rajasthan, India

<sup>c</sup> Laboratory of Molecular Spectroscopy, Kirensky Institute of Physics, Federal Research Center KSC SB RAS, Krasnoyarsk, 660036, Russia

<sup>d</sup> School of Natural Sciences and Mathematics, Ural Federal University, Ekaterinburg, 620026, Russia

<sup>e</sup> I3N-Aveiro, Department of Physics, University of Aveiro, 3810-193, Aveiro, Portugal

## ARTICLE INFO

### Keywords:

Lead-free ceramics  
Raman spectroscopy  
Domain morphology  
Photoluminescence

## ABSTRACT

Present work focuses on detailed temperature-dependent X-ray diffraction, Raman scattering, domain configuration, and photoluminescence (PL) studies in the  $(\text{Ba}_{0.85}\text{Ca}_{0.15})(\text{Zr}_{0.10}\text{Ti}_{0.90})\text{O}_3$  (BCZT) ceramics. The comprehensive Raman spectroscopy analysis in the present work not only validates the presence of the intermediate orthorhombic phase in BCZT, but also provides evidence of another transition: rhombohedral R3c phase to R3m at low temperature. Temperature behaviour of the lowest frequency transverse optical mode (soft E (TO) phonon) and hard modes was studied. Temperature dependence of peak positions, intensities, and linewidths of Raman phonon modes signalled the presence of phase transitions near  $-50 \pm 5$  °C,  $0 \pm 5$  °C,  $35 \pm 5$  °C and  $110 \pm 10$  °C. Evolution of domain morphology occurring at phase transitions above room temperature was studied by piezoresponse force microscopy technique. Analysis of PL spectra revealed disorder/heterogeneity in the sample and indicated the existence of self-trapped excitons. PL spectra are composed of four distinct colour components ( $\sim 2.55\text{eV}$ :blue,  $\sim 2.32\text{eV}$ :green,  $\sim 2.08\text{eV}$ :orange and  $\sim 1.78\text{eV}$ :red).

## 1. Introduction

With the primary objective to discover alternative lead-free piezoelectric materials which can replace lead containing PZT family, the worldwide research has witnessed a tremendous upsurge in the last decade. In this pursuit, among the many non-toxic alternatives, BaTiO<sub>3</sub>-based solid solutions with the morphotropic phase boundary (MPB) composition:  $0.5\text{Ba}(\text{Ti}_{0.8}\text{Zr}_{0.2})\text{O}_3-0.5(\text{Ba}_{0.7}\text{Ca}_{0.3})\text{TiO}_3$  [hereinafter to be referred as BCZT], have been the focus of numerous reports after anomalously high piezoelectric coefficient ( $d_{33} = 620$  pC/N) was reported in the bulk ceramics by Ren et al. [1]. The observation of exceptional  $d_{33}$  was attributed to the MPB that included a triple point at the intersection of paraelectric cubic, ferroelectric rhombohedral, and tetragonal phases [1]. Subsequently, there have been numerous articles on pristine and doped-BCZT ceramics reporting on various studies including piezoelectric, ferroelectric, dielectric, electrostrictive, electrocaloric, energy storage, energy harvesting properties, etc. [2–7]. Besides, there are a few works on Raman studies in BCZT ceramic

composition that is generally related to the comparative studies with dopants at room temperature (RT) or temperature dependence within a small temperature range [8–11]. In the present work, an in-depth temperature-dependent Raman spectroscopy over a much wider temperature range starting from as low as 7 K (–266 °C) to beyond RT has been described and analysed to investigate the existence of possible anomalies in BCZT that have not been explored in any previous work. Among other available methods, Raman spectroscopy is a highly informative and effective tool for the identification of local structural distortions, and low symmetry ferroelectric phases because Raman response is phonon-based and, as a result, is sensitive to the short-range (unit cell level) changes in the structure [12,13]. While, understandably, Raman measurements probe structural features on the local length scale, XRD is best suited for the structure analysis on a larger length scale. Using the complementarity of both techniques, we present a detailed understanding of the evolution of phase transition over a wide temperature range.

Furthermore, there is a dearth of work focussing on the temperature

\* Corresponding author.

E-mail address: [indrani.coondoo@ua.pt](mailto:indrani.coondoo@ua.pt) (I. Coondoo).

<https://doi.org/10.1016/j.ceramint.2020.09.137>

Received 22 August 2020; Received in revised form 13 September 2020; Accepted 13 September 2020

Available online 19 September 2020

0272-8842/© 2020 Elsevier Ltd and Techna Group S.r.l. All rights reserved.

behaviour of domain morphology and the optical properties, particularly on photoluminescence (PL) in pristine BCZT ceramics. Piezoresponse Force Microscopy (PFM) technique which is an established tool that enables non-destructive visualization of domains at nanoscale, was used to comprehend the changes in domain morphology occurring with phase transitions above RT. As far as PL spectroscopy studies are concerned, most articles in literature are primarily centered on rare-earth doped BCZT ceramics [14–16]. In the present work, therefore, an attempt was made to perform temperature-dependent PL studies to probe undoped BCZT ceramics, which have not been explored so far.

### 1.1. Experimental details

$\text{Ba}_{0.85}\text{Ca}_{0.15}\text{Ti}_{0.9}\text{Zr}_{0.1}\text{O}_3$  (BCZT) bulk ceramics were synthesized by the solid-state reaction method via mixing the stoichiometric ratios of  $\text{BaCO}_3$  (99.9%),  $\text{CaCO}_3$  (99%),  $\text{TiO}_2$  (99%), and  $\text{ZrO}_2$  (99%). Initial heat treatment included calcination at 1200 °C for 6 h. The cylindrical pellets were fabricated by uniaxially pressing the calcined powder and were subjected to sintering at 1450 °C for a dwelling time of 2 h.

The microstructure was assessed by Field Emission Scanning Electron Microscopy (FESEM, Hitachi S-4100). X-ray diffraction was performed on a Phillips X'Pert diffractometer (Almelo, Netherlands), using  $\text{Cu K}\alpha$  radiation in the range  $20^\circ \leq 2\theta \leq 80^\circ$  and for temperatures between  $-100^\circ\text{C}$  and  $130^\circ\text{C}$ . Raman spectra in the  $180^\circ$  geometry were recorded with a Horiba Jobin Yvon T64000 spectrometer equipped with a liquid nitrogen-cooled charge-coupled device detection system in subtractive dispersion mode.  $\text{Ar}^+$  ion laser (Spectra-Physics Stabilite 2017) with  $\lambda = 514.5$  nm and power 5 mW was used as an excitation light source. Spectroscopic low-wavenumber measurements were performed in the subtractive dispersion mode, which attained a low-wavenumber limit of  $8\text{ cm}^{-1}$  in the present setup. The deformation of the low wavenumber spectral edge by an optical slit, which sometimes smears the real features of low-wavenumber spectra, was carefully eliminated by rigorous optical alignment. Temperature-dependent measurements were carried out with a closed-cycle ARS CS204-X1. SS helium cryostat in the temperature range 7–410 K ( $-266$  to  $136^\circ\text{C}$ ). The temperature was monitored by a LakeShore DT-6SD1.4 L silicon diode, having a temperature stabilization accuracy  $\sim 0.1$  K. The sample was placed on an indium pad open at one side and fixed to the cold finger of the cryostat. During the data acquisition, a vacuum of  $10^{-6}$  mBar was maintained in the cryostat. Regarding the interpretation of results, data has been represented in terms of degrees Celsius instead of the Kelvin scale.

For PFM observations, the as-sintered sample was rigorously polished. Mechanical stress induced by polishing was relieved by annealing the pellet at  $400^\circ\text{C}$  in air for 2 h followed by very slow cooling. PFM investigations were performed using a commercial Atomic Force Microscope (MFP-3D, Asylum Research, Oxford Instruments, UK), equipped with a high-temperature module. The vertical PFM (VPFM) signal was acquired in Dual AC Resonance Tracking (DART) mode at the contact resonance frequency of cantilever ( $\approx 300$  kHz) and 1 V amplitude. Scansens commercial cantilevers with  $\text{W}_2\text{C}$  tip coating with a typical curvature radius of about 35 nm (as specified by the manufacturer) were used.

For photoluminescence measurements, a homemade setup consisting of He–Cd laser (325 nm) and monochromator (SPEX 1701/02) assembly placed in orthogonal geometry was used. Emission from the sample placed between the laser and monochromator was collimated and converged into a tiny spot to enter the monochromator. A notch filter was used to allow only the emission radiation and discard the reflected laser radiation. A thermoelectrically cooled photomultiplier tube receives and detects the signal from the monochromator. For low-temperature PL measurements, the sample was mounted in a liquid helium closed-cycle cryostat to adjust the temperature from 20 to 150 K using a temperature controller.

## 2. Results and discussion

### 2.1. Grain morphology and compositional determination

Prior to any characterization, an investigation of the quality and morphological features of the prepared ceramic was undertaken. Fig. 1a depicts the SEM image of the as-sintered surface of BCZT generated using the secondary electrons. A dense microstructure with a wide grain size distribution is revealed. An estimated average grain size  $\sim 27 \pm 0.67\ \mu\text{m}$  was obtained. The measured apparent bulk density value was  $\sim 5.54\ \text{g/cm}^3$  which is  $\sim 95.8\%$  of the theoretical density ( $5.78\ \text{g/cm}^3$ ). To ascertain the compositional homogeneity, elemental distribution within the ceramic matrix was characterized using energy-dispersive x-ray analysis (EDX), as shown in Fig. 1b. Quantification of the constituent elements was done using EDX analysis data, which revealed that the atomic percentage of elements is in good approximation to the expected values in the nominal composition of the studied BCZT system (inset of Fig. 1b). The experimental values are indicated in the figure along with the theoretical values in parenthesis. Fig. 1c delineates the distribution mapping of all the constituent elements (Ba, Ca, Zr, Ti, and O) within the ceramic bulk of the corresponding micrograph (Fig. 1a), unveiling a highly homogenous distribution. The elemental mapping images as seen in Fig. 1(d–h) depict that the individual elements are evenly distributed at a local scale.

### 2.2. X-ray diffraction

Interpretation of XRD, in particular with the reference to BCZT has never been unanimous regarding its structural state, likely due to probable causes: (a) “pinching” of orthorhombic symmetry by the approaching *R* and *T* phases [17], (b) nearly similar pseudo-cubic lattice parameters of *Amm2* and *R3m* phases [18]. To determine the phase composition in the present BCZT sample, Rietveld refinement of the XRD data was performed using different phase combinations including tetragonal *P4mm* (*T*), orthorhombic *Amm2* (*O*), and rhombohedral *R3m* (*R*) symmetries. Standard GSAS refinement software [19] with a graphical interface EXPGUI [20] was utilized for fitting. The fitted XRD pattern for the tri-phase model considering all the three phases together (*P4mm* + *Amm2* + *R3m*) is shown in Fig. 2. The Rietveld refinement agreement factors are enlisted in Table 1.

In addition, refinement using a single-phase orthorhombic and single-phase tetragonal system was also carried out, which resulted in a poor fit. The two-phase *R3m* + *Amm2* model did not result in a stable refinement. As one can see, the refinement agreement factors for the *R3m* + *P4mm* model are principally more acceptable than the rest, owing to the minimum  $\chi^2$  value. Therefore, it seems reasonable to infer that the crystallographic state at room temperature in the BCZT compound is characterized by the co-existence of two ferroelectric phases with space groups *P4mm* (tetragonal) and *R3m* (rhombohedral). However, one must take into consideration that the refinement software can get minimum chi-square with several different combinations of the FWHM and lattice parameters, and there is always a possibility that the refinement is trapped in local minima. In other words, the FWHM and lattice parameters of the phases can influence fitting of the high-intensity peaks slightly better, while  $\chi^2$  is not much affected by misfits of weak intensity peaks. Consequently,  $\chi^2$  cannot be the best criterion in such situations. Hence, even though  $\chi^2$  is lowest with the *T* + *R* model; its XRD profile shows clear misfit regions, as perceptible from the magnified {111} and {200} peaks (Fig. 3a and b). Similarly, the *O* + *T* model also exhibits misfit regions (Fig. 3c and d). Indeed, excellent quality of the fit to the observed pattern of low angle peaks is evident with the inclusion of the *A2mm* phase in the structural analysis (*T* + *O* + *R* model) as can be seen in Fig. 3e, f. Based on these observations, it is concluded that the room temperature phase of the BCZT system is characterized by the co-existence of *P4mm* + *Amm2* + *R3m* symmetries.

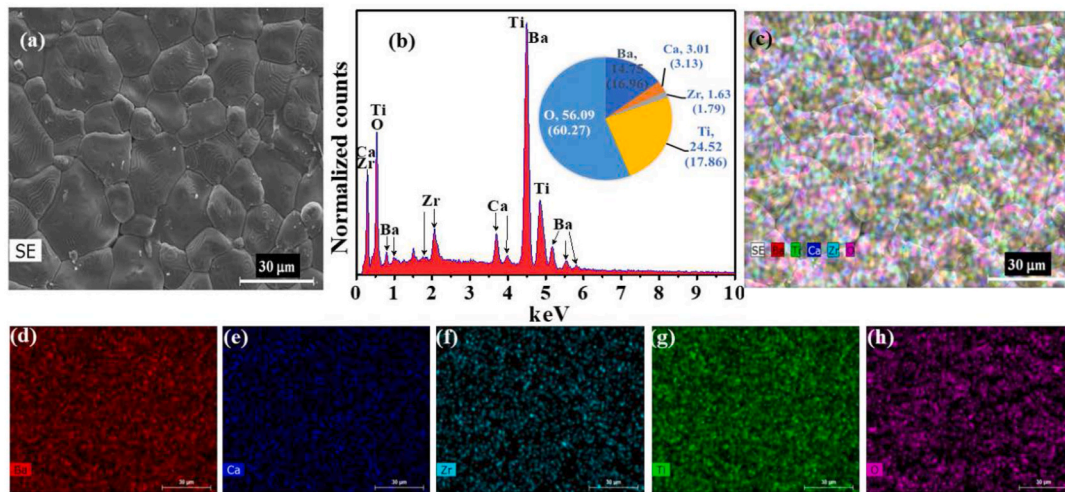


Fig. 1. (a) SEM micrograph (b) EDX spectrum and inset depicts the atomic percentage of elements along with expected values (in parenthesis) (c–h) elemental mapping corresponding to micrograph (a), of the BCZT system. Scale bar in (d–h) is 30  $\mu\text{m}$ .

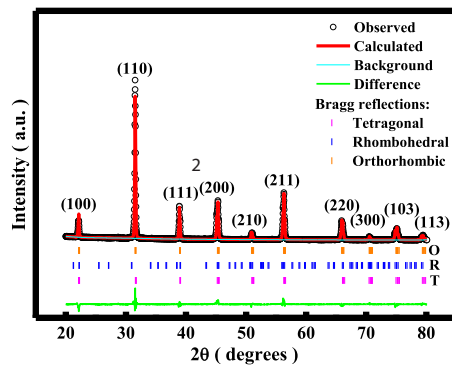


Fig. 2. (Colour online) Fitted powder diffraction patterns obtained by Rietveld refinement using  $P4mm + Amm2 + R3m$  space group combinations. The small vertical bars above the difference profile indicate the positions of Bragg reflections ( $T$ : tetragonal;  $O$ : orthorhombic and  $R$ : rhombohedral phase).

The weight fractions of  $P4mm$ :  $Amm2$ :  $R3m$ , as obtained from the Rietveld analysis, were found to be 59:29:12. The unit cell and structural parameters, extracted from the Rietveld crystal structural refinement of BCZT for the  $P4mm + Amm2 + R3m$  model, are presented in Table 2.

Fig. 4 demonstrates the XRD profiles of a few selected Bragg reflections ( $\{200\}$ ,  $\{220\}$  and  $\{222\}$ ), between  $-100$  and  $130$   $^{\circ}\text{C}$ . Noticeable changes can be observed in the profile shapes and positions at different temperatures. The rhombohedral phase, which is characterized by a doublet  $\{222\}$ , can be visualized at  $-100$   $^{\circ}\text{C}$ . The  $R3m$  distortion splits the  $\{222\}$  peak into two peaks with rhombohedral Miller indices being  $(222)_R$  and  $(22-2)_R$ . On further heating, the next

transition is evident at  $-10$   $^{\circ}\text{C}$ . For instance, a hump develops on the right of the main peak in  $\{200\}$  profile at  $-10$   $^{\circ}\text{C}$  marking a transition into the orthorhombic phase. Likewise, we note a change in the  $\{222\}$  profile at  $-10$   $^{\circ}\text{C}$ , where the doublet related to the orthorhombic phase can be seen. Concerning the  $Amm2$  phase, the two orthorhombic peaks have the indices  $(240)_O$  and  $(204)_O$ . These doublets with nearly equal intensity for  $Amm2$  appear in the immediate proximity on either side of the tetragonal  $(222)_T$  peak at  $30$   $^{\circ}\text{C}$ , as is evident from Fig. 4. For the  $P4mm$  structure, the  $\{222\}$  peak is a singlet. Additionally, distinct changes are perceptible at  $30$   $^{\circ}\text{C}$  in all the profiles, indicating a clear transformation into the tetragonal phase. Also, it may be worth noting that rhombohedral  $(22-2)_R$  and the orthorhombic peak  $(204)_O$  both appear on the right side of the tetragonal  $(222)_T$  and overlap. However, the distinct separation of  $(222)_R$  and  $(240)_O$  peaks serves as a guide to ascertain the presence of  $R3m$  and  $Amm2$  phases, respectively, in BCZT [18]. Similarly, noticeable changes are perceptible in the evolution of a  $\{200\}$  profile.

### 2.3. Raman spectroscopy

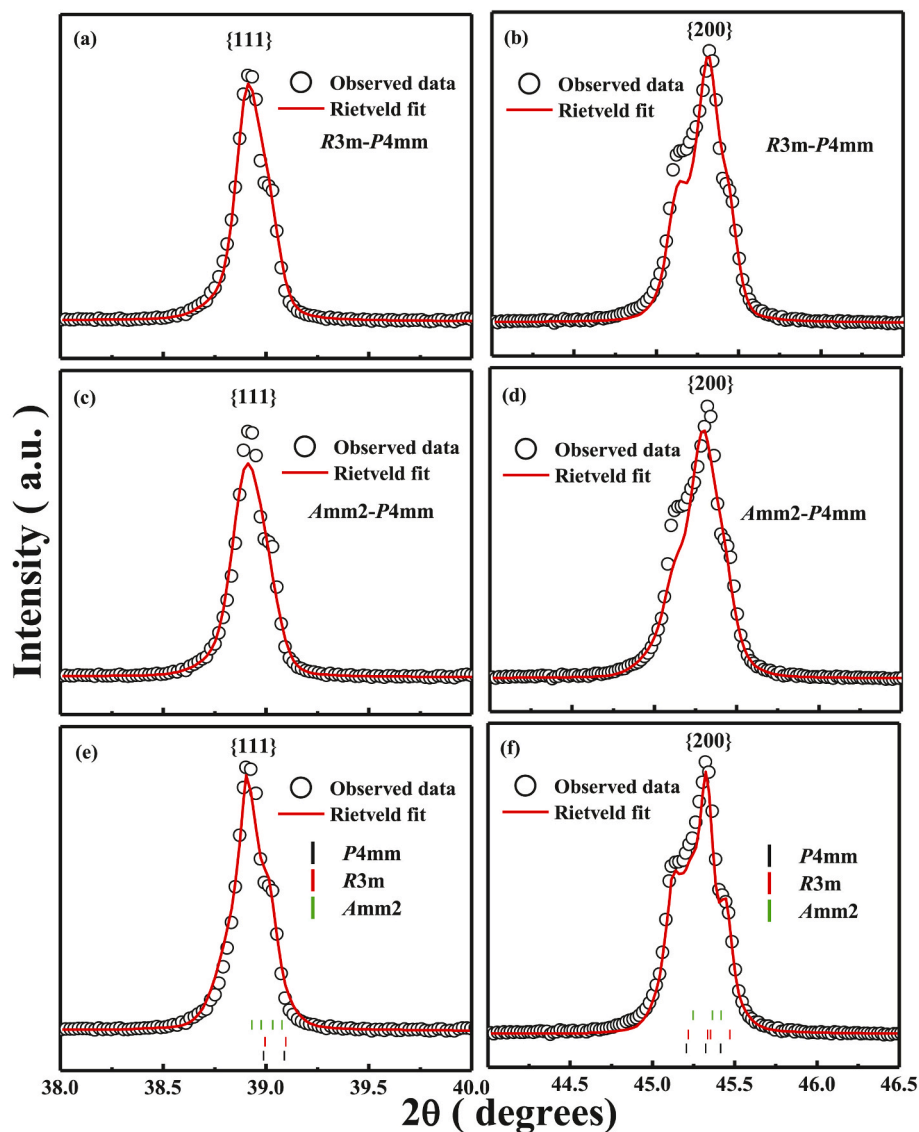
#### 2.3.1. Evolution of Raman spectra with temperature

Fig. 5a illustrates the Raman scattering spectrum obtained at room temperature in the wavenumber range  $20$ – $1000$   $\text{cm}^{-1}$ . The spectrum has been de-convoluted into its characteristic vibration bands and assigned to their respective phonon modes based on the observed modes in the Raman spectrum of BTO [21,22]. Typically, the phonon modes in a tetragonally distorted ferroelectric phase ( $P4mm$  space group) in BTO are represented as:  $3 [A_1(\text{TO}) + A_1(\text{LO})] + B_1 + 4 [E(\text{TO}) + E(\text{LO})]$  [23]. In the present BCZT compound, the spectrum includes all modes allowed by Raman selection rules; however, except for the forbidden prominent peak near  $555$   $\text{cm}^{-1}$  (marked '#') and broadening of bands

Table 1

Rietveld agreement factors and phase composition of BCZT performed for different models ( $T + R$ ;  $T + O$  and  $T + R + O$ ). Values in parentheses give the standard deviations.

Agreement factors					Phase compositions (wt. %)		
No. of variables	$R_F^2(\%)$	$R_{wp}(\%)$	$R_p(\%)$	$\chi^2$	Tetragonal ( $P4mm$ )	Rhombohedral ( $R3m$ )	Orthorhombic ( $Amm2$ )
23	6.53	9.23	6.82	5.52	75.67 (5)	24.33 (9)	–
19	8.94	10.56	7.9	9.45	81.96 (1)	–	18.04 (4)
23	8.11	9.757.19	6.34	58.91 (1)	12.08 (4)	29.01 (8)	–



**Fig. 3.** (Colour online) Rietveld fitted x-ray powder diffraction profiles of low-angle pseudocubic  $\{111\}$  and  $\{200\}$  reflections fitted with different models. (For interpretation of the references to colour in this figure legend, the reader is referred to the Web version of this article.)

associated with compositional disordering. The otherwise strong spectral dip observed in BTO near  $180\text{ cm}^{-1}$  [12] and understood as a result of the anti-resonance effect owing to anharmonic coupling among three  $A_1$  (TO) phonons, is less pronounced in the BCZT composition. Moreover, the band at  $\sim 308\text{ cm}^{-1}$ , which is considered as a signature of the tetragonal phase at room temperature, is no longer a sharp peak (as in BTO) and appears as a weak broad shoulder band in BCZT. Dominant  $A_1$  (TO) character is evident for the peaks observed near  $265\text{ cm}^{-1}$  and  $520\text{ cm}^{-1}$ ; the former being associated with polar Ti–O vibrations while the latter is related to distortion in the  $\text{TiO}_4$  plane and bending of the Ti ion and apical oxygen atoms. Observation of phonon mode at  $555\text{ cm}^{-1}$  has been reported previously in other BTO-based compositions as well [21, 24, 25]. Generally, additional phonon modes appear owing to size effects, change in inter-atomic forces due to chemical substitution and high mechanical pressure which causes disorder in the position of Ti atoms that breaks the Raman selection rules [21, 26–28]. The characteristic LO mode at  $\sim 725\text{ cm}^{-1}$  is due to the bending and stretching of  $\text{BO}_6$  octahedra giving it a mixed  $A_1$  and  $E$  character. The appearance of an additional phonon mode at  $751\text{ cm}^{-1}$  (marked ‘§’), is splitting of the

LO mode attributed.

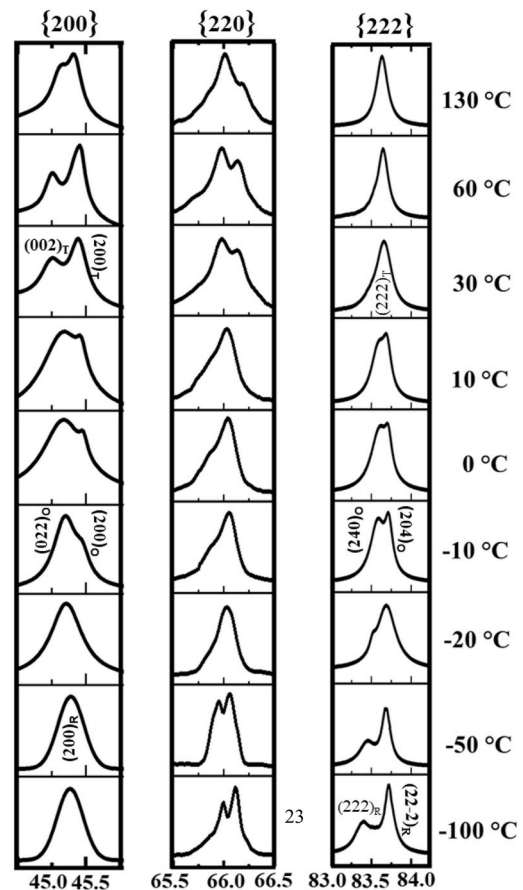
To the heavier Zr substitution [29–31]. An alternative explanation for the occurrence of mode at  $750\text{ cm}^{-1}$  was provided by Lazarevic et al. [32], who claimed it to be due to the multiphonon process. The broad mode at  $\sim 800\text{ cm}^{-1}$  ( $A_{1g}$ ) is an octahedral breathing-like mode resulting from the presence of two or more B-site species [33] and it may appear regardless of the presence or absence of a ferroelectric phase [29].

Fig. 5 (b) represents the evolution of Raman spectra with temperature collected between  $-266\text{ }^\circ\text{C}$  and  $410\text{ }^\circ\text{C}$ , while Fig. 5c illustrates deconvoluted spectra for a few selected temperatures. Peak positions were estimated by fitting the data with Gaussian components. Inset of Fig. 5b displays the magnified view of the low wavenumber region  $20\text{--}400\text{ cm}^{-1}$  for temperatures between  $-266\text{ }^\circ\text{C}$  and room temperature. It may be noted that, since most features of the modes in the R phase include those from O and/or T phase and given the complexity of BCZT crystal structure, it becomes difficult to exclude the existence of the latter or both phases. Nonetheless, the characteristic evolution with increasing temperature, like gradual softening of the main modes together with broadening and simultaneous loss of intensity/complete disappearance

**Table 2**

Unit cell and structural parameters as obtained from the Rietveld crystal structural refinement of BCZT for the  $P4mm + Amm2 + R3m$  model.

Unit cell parameters	Atomic coordinates					
	Atoms	Wyckoff position	X	Y	Z	Uiso (Å <sup>2</sup> )
Tetragonal (space group: $P4mm$ )	Ba/Ca	1a	0.000	0.000	0.000	0.34 (7)
$a = b =$ 3.9845 (1) Å	Ti/Zr	1b	0.500	0.500	0.413 (1)	0.12 (6)
$c = 4.0018$ (2) Å	O1	1b	0.500	0.500	0.314 (1)	0.39 (2)
$c/a = 1.004$	O2	2c	0.500	0.000	0.517 (2)	0.27 (3)
$\alpha = \beta = \gamma =$ 90°						
Volume = 63.534 Å <sup>3</sup>						
Rhombohedral (space group: $R3m$ )	Ba/Ca	3a	0.000	0.000	0.000	0.8 (5)
$a = 5.7756$ (2) Å	Ti/Zr	3a	0.000	0.000	0.485 (2)	0.07 (9)
$\alpha = \beta = \gamma =$ 87.34°	O	9b	0.478 (5)	0.522 (1)	0.067 (9)	0.37 (7)
Volume = 192.069 Å <sup>3</sup>						
Orthorhombic (space group: $Amm2$ )	Ba/Ca	2a	0.000	0.000	0.000	0.12 (4)
$a = 3.9841$ (2) Å	Ti/Zr	2b	0.500	0.500	0.517 (2)	0.33 (6)
$b = 5.6593$ (5) Å	O1	2a	0.000	0.000	0.491 (4)	0.38 (7)
$c = 5.6501$ (6) Å	O2	4e	0.500	0.256 (4)	0.236 (7)	0.13 (2)
$\alpha = \beta = \gamma =$ 90°						
Volume = 127.395 Å <sup>3</sup>						



**Fig. 4.** Evolution of the reflection peaks in the {200}, {220} and {222} profile as a function of temperature. Miller indices of the distinct peaks in {200} and {222} profiles are marked.

of the modes with increasing temperature, aid in conjecturing the phase transitions. It is evident that for temperatures lower than  $-10$  °C, the BCZT system exhibits rhombohedral phase, verifiable by the presence of sharp modes in the low-wavenumber region and supported by the coexistence of the so-called ‘triple mode’ (features 2, 4 and 5 in Fig. 5b and c); absence of the overdamped soft mode, and presence of peak  $\sim 495$   $\text{cm}^{-1}$  [E (TO4)]. These characteristic features of the rhombohedral phase have been previously reported in other BTO-based compositions like  $\text{Ba}(\text{ZrxTi}_{1-x})\text{O}_3$  and/or  $\text{Ba}(\text{SnxTi}_{1-x})\text{O}_3$  [29,34–37]. The presence of peak 2 at  $\sim 115$   $\text{cm}^{-1}$  is related to Zr–O motion in the structure and is a signature of the existence of Zr-based domains with a local rhombohedral-type structure, and the other spectral dip near 130  $\text{cm}^{-1}$  is an interference effect between A1 (TO) phonons and appears when two chemically different  $\text{BO}_6$  octahedral clusters coexist [33,38]. With an increase in temperature, significant changes can be observed. As seen in the inset of Fig. 5b, peak 6 gradually broadens while peak 5 is gaining strength. Also, the [E (TO4)] mode loses intensity by  $-50$  °C. Additionally, Peak 1 steadily weakens and subsequently disappears by  $-50$  °C (Fig. 5b; inset in 5b, and 5c). It is worthwhile mentioning at this point, that the observation of a phonon mode near 60–70  $\text{cm}^{-1}$  (peak 1) has not been reported for  $\text{BaTiO}_3$ . However, activation of this phonon mode has been well-documented in a similar perovskite, PZT [39–41]. In the present case, it is possibly, as in PZT, an indication of a transition from low-temperature rhombohedral phase with symmetry  $R3c$  to high-temperature rhombohedral  $R3m$  phase. Distinguishing evolution observed in the transition  $R3c \rightarrow R3m$  is reflected in the reinforcement of peak 5 as opposed to peak 6 and loss of peak 1. From the viewpoint of

symmetry, the transition  $R3c \rightarrow R3m$  is accompanied with an instability of the Brillouin zone corner causing an altered oxygen octahedral tilt and resulting in a doubling of primitive cell [42,43]. This transition can be seen in XRD only as superlattice reflections, which is not in this case. With further increase in temperature, (a) the subtle appearance of mode [E (LO3), A1 (LO2)] at  $\sim 470$   $\text{cm}^{-1}$ , (b) materialization of mode [E (TO2), E (LO1)] at  $\sim 178$   $\text{cm}^{-1}$ , (c) drastic reduction in the intensity of mode 5 i.e. [A1 (LO1)] and (d) disappearance of peak 2 (Fig. 5c) at  $-10$  °C signal a transition to the orthorhombic phase. In proximity to room temperature, the sharpening of [E (LO2)] mode (comprehensible in Fig. 5c), together with the disappearance of interference dip at  $\sim 180$   $\text{cm}^{-1}$  and dissolution of the intensity gaps between features 3–4 and 4–5 (Fig. 5b and inset), indicates transition to the tetragonal phase. A coexistence of R-, O- and T-type phases cannot be excluded at this temperature. The A1 (TO) and [A1 (LO), E (LO)] modes near 520  $\text{cm}^{-1}$  and 725  $\text{cm}^{-1}$ , respectively, can be assigned to phase structure with either R, O or T symmetry [44] and references therein]. Therefore, in accordance with room-temperature XRD results, the coexistence of R, O and T symmetries is indicated here as well. The Raman spectrum for temperatures  $\geq 110$  °C (Fig. 5b and c) is distinguished by (a) significant drop in the intensity and broadening of the asymmetric band in the vicinity of 520  $\text{cm}^{-1}$ , (b) emergence of all the modes in low-frequency region as a broad hump and (c) disappearance of peaks in the region 700–800  $\text{cm}^{-1}$ . These changes irrefutably indicate the T  $\rightarrow$  C transition. In general, the persistence of the modes that are theoretically forbidden in the cubic phase implies that this polymorph does not have perfect cubic symmetry and retains some disorder, which breaks the symmetry locally

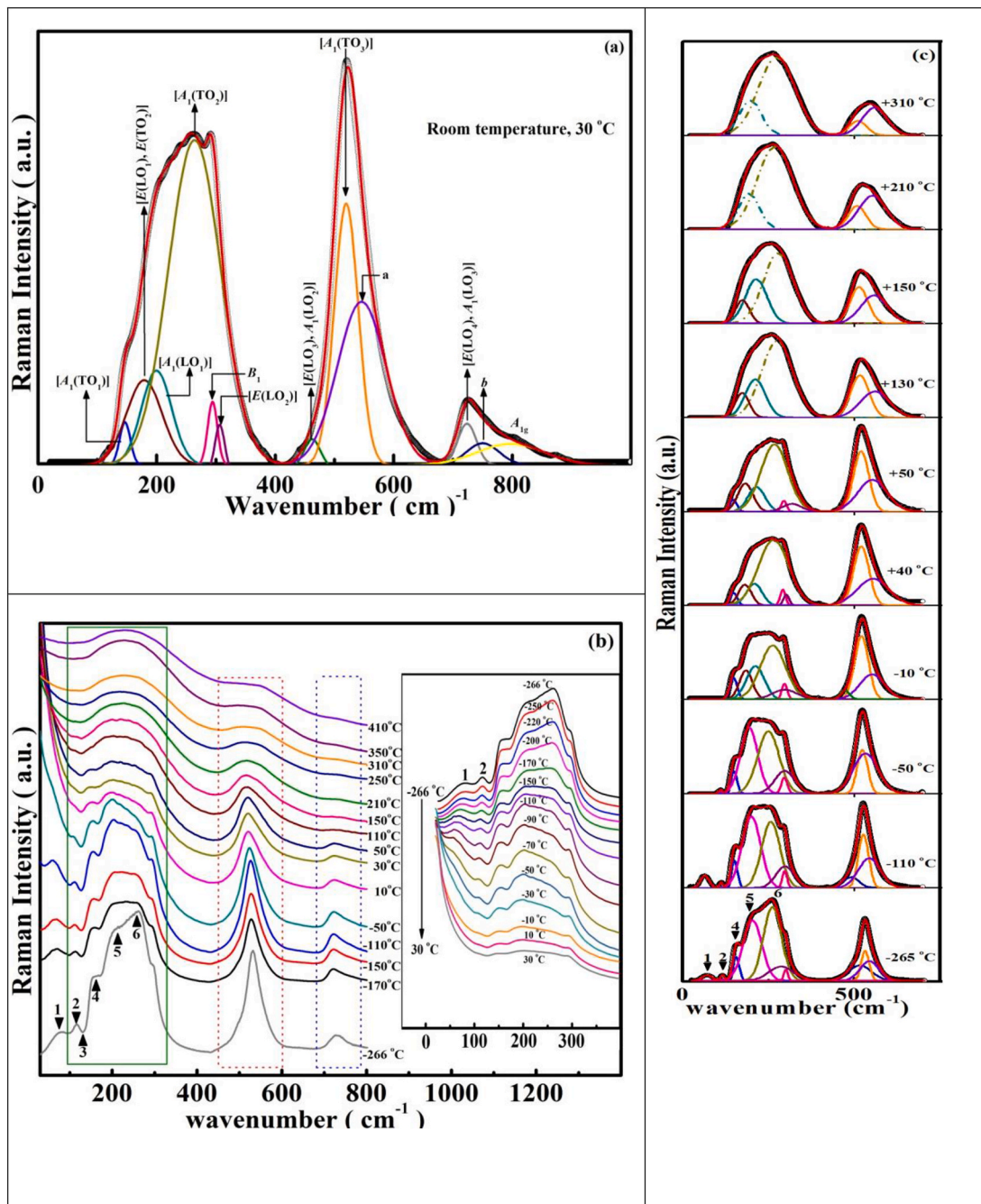


**Fig. 5.** (Colour online) (a) De-convoluted Raman spectrum at room temperature (b) Temperature evolution of Raman spectra in BCZT recorded between - 266 °C and 410 °C. Inset shows magnified region of Raman spectra between 10 and 400  $\text{cm}^{-1}$  comprising spectra obtained between -266 and 30 °C and (c) de-convoluted spectra fitted with Gaussian components.

and permits first-order Raman scattering [45]. More accurately, it is associated with the presence of local dynamic polar clusters in the cubic structure associated with the lattice disorder related to the positions of Ti ions along the cube diagonals [34].

**2.3.2. Temperature dependence of bandwidth, frequency shift and intensity of Raman modes**

The qualitative trends described in the preceding section can be interpreted more accurately from the variations in the temperature evolution of the Raman band parameters, namely frequency shift, intensity and linewidth of the optical phonon lines. In this regard, the dynamic behaviour of the lowest frequency transverse optical mode

(soft  $E$  (TO) phonon), which is responsible for the lattice instability at the phase transition, has been of major interest in ferroelectric materials [46]. However, as can be seen from Fig. 5, the characteristic soft mode for BTO ( $E$  (TO) phonon at  $\sim 35 \text{ cm}^{-1}$ ) is highly overdamped in this case. To quantitatively analyze the temperature dependence of the peak at the lowest wavenumber (near  $70 \text{ cm}^{-1}$  in the present case), Raman spectra were fitted with a combination of conventional damped harmonic oscillator (DHO) type phonon function corrected for the Bose-Einstein temperature factor [47]:

$$I(\omega) = F(\omega, T) \cdot \sum_i \frac{2A_i \omega_{0i}^2 \gamma_i \omega}{(\omega_{0i}^2 - \omega^2)^2 + 4\gamma_i^2 \omega^2}$$

where  $A$ ,  $\omega_0$  and  $\gamma$  denote the intensity, harmonic wavenumber and damping constant, respectively, of the corresponding excitation indicated by the subscript. The temperature factor  $F(\omega, T)$  is calculated by Ref. [47]:

$$F(\omega, T) = \begin{cases} n(\omega) + 1 (\text{Stokes part}) \\ n(\omega) (\text{anti-Stokes part}) \end{cases}$$

$$n(\omega) = \left[ \exp\left(\frac{\hbar\omega}{k_B T}\right) - 1 \right]^{-1},$$

where  $\hbar$  and  $k_B$  are the reduced Planck's constant and the Boltzmann constant, respectively.

Fig. 6 illustrates the dynamics of this lowest wavenumber. The behaviour was studied considering it to be the soft mode whose wavenumber is described by  $\omega_s (= \sqrt{\omega_{0s}^2 - \gamma_s^2})$  [48]. Since  $\omega_s$  becomes overdamped in a wide temperature range (hatched area), the effective wavenumber,  $\omega_{eff} (\equiv \omega_{0s}^2 / \gamma_s)$  was calculated instead and its temperature variation is shown in Fig. 6. With increasing temperature,  $\omega_{eff}$  initially decreases, then levels off near  $T_c$  and thereafter hardens. Analysis reveals that this vibrational line near  $70 \text{ cm}^{-1}$  does not exhibit pure soft mode behaviour for which the frequency should exhibit its minimum at  $T_c$  [49].

In contrast to the investigation of soft modes, it has been shown that hard mode spectroscopy is even more powerful for the analysis of phase changes under structure transformations [50]. Since the characteristic length of high-frequency phonons is very short, any short-range static and/or dynamic change in structure is expected to show systematic modulations in terms of the slope changes in their band characteristics [50,51]. Therefore, high wavenumber region ( $400 - 900 \text{ cm}^{-1}$ ) was studied in greater detail by using very small temperature intervals between the measurements ( $0.4 \text{ }^\circ\text{C}$ ). The most pertinent band characteristics are presented in the following discussions. Fig. 7 summarizes the results for the transverse optical Raman modes at  $\sim 495 \text{ cm}^{-1}$  [ $E(\text{TO}_4)$ ],  $\sim 525 \text{ cm}^{-1}$  [ $A_1(\text{TO}_3)$ ], and  $\sim 555 \text{ cm}^{-1}$  that clearly demonstrate the signatures of phase transitions seen as discontinuities and slope changes in the temperature evolution of their intensity, line width and wavenumber. Fig. 7a illustrates the temperature dependence of normalized intensity for the modes at  $\sim 495 \text{ cm}^{-1}$  and  $525 \text{ cm}^{-1}$ . The temperature anomalies suggesting phase transformations are marked by dotted-dashed vertical lines in this plot. The intensity of vibration mode (at  $\sim 495 \text{ cm}^{-1}$ ) is found to continuously weaken with increasing temperature, and gradually falling to zero at around  $-50 \text{ }^\circ\text{C}$ . Signature of the  $T$ - $C$  phase transition is apparent with the loss of intensity of the phonon mode [ $A_1(\text{TO}_3)$ ] at a temperature  $130 \text{ }^\circ\text{C}$ , which is higher than that

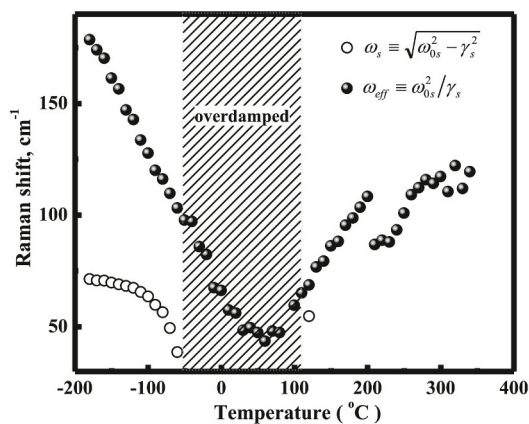


Fig. 6. Analysis of the lowest vibrational line at  $\sim 75 \text{ cm}^{-1}$  in terms of soft mode wavenumber ( $\omega_s$ ) and effective wavenumber ( $\omega_{eff}$ ).

obtained by dielectric measurement. In addition, slope changes were perceptible at  $\sim 0 \text{ }^\circ\text{C}$  and  $\sim 35 \text{ }^\circ\text{C}$  also. Since the intensity of the vibrational line at  $525 \text{ cm}^{-1}$  is known to be proportional to the dielectric anomaly through the fluctuation-dissipation theorem [52,53], it is worth studying its intensity variation for the entire temperature range. The same is depicted in Fig. 7b. As seen, this mode is present across the entire temperature range, gradually losing strength and finally disappearing at  $\sim 130 \text{ }^\circ\text{C}$ . Moreover, the detectable slope changes are in close agreement with the anomalies observed in the dielectric properties of BCZT samples. It may be noted that, both the transitions ( $R \rightarrow O$  and  $O \rightarrow T$ ) are corroborated by an inflection in the loss tangent and permittivity curves (Fig. 7b), however the transitional event ( $R3c \rightarrow R3m$ ) is not reflected in the dielectric measurements; a fact being often observed in ferroelectrics wherein phase transitions affect properties like elastic or Raman modes but are not mirrored in their dielectric response [11]. The small discrepancy between the Curie-temperature values is due to the difference in coherence length (spatial magnitude) and time scale of the physical phenomenon measured by the two techniques. For Raman investigation, it is much smaller in comparison to dielectric measurements. Moreover, the incomplete  $T \rightarrow C$  transition at the dielectric Curie temperature and presence of residual ferroelectric symmetry into the cubic phase is well-documented and already discussed in the preceding section. At this point, there is another observation worth noting in Fig. 7b which is related to the broad maximum in loss tangent curve in the temperature range  $-200$  to  $-75 \text{ }^\circ\text{C}$ . The  $\tan\delta$ -peak was observed to shift towards higher temperatures with increasing frequency, implying a thermally activated process (figure not shown here). The behaviour was parameterized by fitting the data using both: the simple Arrhenius-type empirical relation and the more complex 'freezing' process described by the Vögel-Fulcher model. Best fit was obtained using the Vogel-Fulcher model that yielded fitting parameters:  $f_0 = 1.75 \times 10^7 \pm 3 \text{ Hz}$ ,  $E_a = 1.26 \pm 0.41 \text{ meV}$  and  $T_{VF} = -140.64 \pm 4.74 \text{ }^\circ\text{C}$ , and good quality of fit determined by a reduced  $\chi^2 = 0.19516$ . The low-temperature relaxation phenomenon in the studied BCZT sample was attributed to the local relaxation process within the  $R$  phase.

In Fig. 7c, the temperature dependence of frequency shift in vibrational lines  $\sim 496 \text{ cm}^{-1}$  and  $\sim 555 \text{ cm}^{-1}$  clearly indicates phase transitions near  $-50 \text{ }^\circ\text{C}$  and  $0 \text{ }^\circ\text{C}$ , respectively. Fig. 7d demonstrates the temperature variation of the bandwidth (FWHM) of the studied modes. Distinct slope changes are perceptible and are marked accordingly in the figure. Raman and dielectric results are merged to elucidate the correlation between them. The phonon mode near  $555 \text{ cm}^{-1}$  initially broadens as the temperature is raised, then shows a slope change near  $-5 \text{ }^\circ\text{C}$  and  $\sim 40 \text{ }^\circ\text{C}$ . Whereas, mode  $A_1(\text{TO}_3)$  exhibits slope changes near  $-50 \text{ }^\circ\text{C}$  and  $\sim 40 \text{ }^\circ\text{C}$ . On the other hand,  $E(\text{TO}_4)$  mode weakens as the temperature increases and is finally lost near  $-50 \text{ }^\circ\text{C}$ .

In a nutshell, the detailed analysis of Raman results provides the evidence of four phase transitions in the studied BCZT system at:  $-50 \pm 5 \text{ }^\circ\text{C}$ ,  $0 \pm 5 \text{ }^\circ\text{C}$ ,  $35 \pm 5 \text{ }^\circ\text{C}$ , and  $110 \pm 10 \text{ }^\circ\text{C}$ . Modulations near  $-50 \text{ }^\circ\text{C}$  are assigned to the transition from the low-temperature  $R$  phase into another  $R$  phase ( $R3c \rightarrow R3m$ ). The subsequent transition observed close to  $0 \text{ }^\circ\text{C}$  marks the transition  $R \rightarrow O$  and the following phase transition is identified as transformation  $O \rightarrow T$ . The ultimate transition in the phase sequence represents the *ferro-paraelectric* transition, observed near  $\sim 110 \pm 10 \text{ }^\circ\text{C}$ .

#### 2.4. Piezoresponse force microscopy (PFM)

To explore the temperature-induced modifications in the domain morphology of the BCZT ceramic sample, temperature-dependent PFM measurements were conducted for the sample that was continuously heated and cooled at the rate  $5 \text{ }^\circ\text{C}/\text{min}$ . The measurements were performed in a Dual AC Resonance Tracking (DART) mode to gain resonance amplification. A representative area  $15 \times 15 \text{ } \mu\text{m}^2$  of the sample was explored as shown in Fig. 8a. The topography image shows the

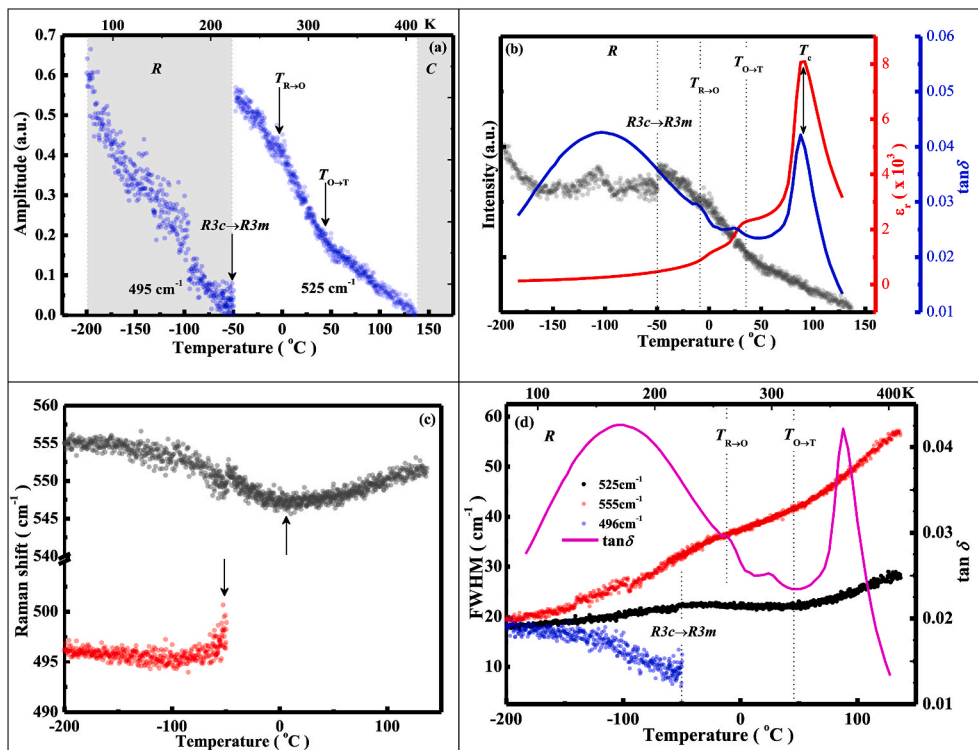


**Fig. 7.** (Colour online) (a) Temperature evolution of the normalized intensity of [A<sub>1</sub> (TO<sub>3</sub>)] and [E (TO<sub>3</sub>)] phonon modes (b) comparative between phase transitions observed as anomalies in dielectric properties and slope changes in the intensity of [A<sub>1</sub> (TO<sub>3</sub>)] mode. Temperature dependence of (c) peak position and (d) linewidth of few vibrational lines in the 400–600 cm<sup>-1</sup> wavenumber range. In (d) tangent loss curve is also included for comparison. The distinct regions are separated by dashed lines.

typical defects: grain boundaries and pores, characteristic for a sintered polycrystalline ceramic. Fig. 8(b–f) display piezoresponse amplitude images acquired at different temperatures (heating and cooling cycles). At room temperature, domains appear as alternating bands with a combination of bright and dark contrasts representing alternating polarization directions from one domain to its immediate neighbour. The right-angled lamellar structure observed in Fig. 8b is a typical feature of the domain structure in BaTiO<sub>3</sub> ceramics having tetragonal symmetry. Additionally, blotched regions with a considerable out-of-plane piezoresponse were also found (marked as a boxed region in Fig. 8b). Based on XRD results, it is believed that the blotched region at ambient

temperature consists of complex nano-lamellae of orthorhombic/rhombohedral-phases in the tetragonal matrix. Development of the domains corresponding to the R3m phase must occur within the already existing complex orthorhombic domains, which are grown in the pre-existing tetragonal domains. Such a complex domain structure with the co-existence of irregular nano-domains along with regular domains has been reported in the two-phase (R-T) coexisting state in 0.96 (K<sub>0.4</sub>Na<sub>0.6</sub>) (Nb<sub>0.96</sub>Sb<sub>0.04</sub>)O<sub>3</sub>-0.04Bi<sub>0.5</sub>K<sub>0.5</sub>Zr<sub>0.85</sub>Sn<sub>0.15</sub>O<sub>3</sub> ceramics [54]. Moreover, *in-situ* cooling TEM observation has shown the development of miniaturized R-nanodomains inside the T-domain lamellas of BZT-0.5BCT ceramic when it was cooled down to 25 °C [55].

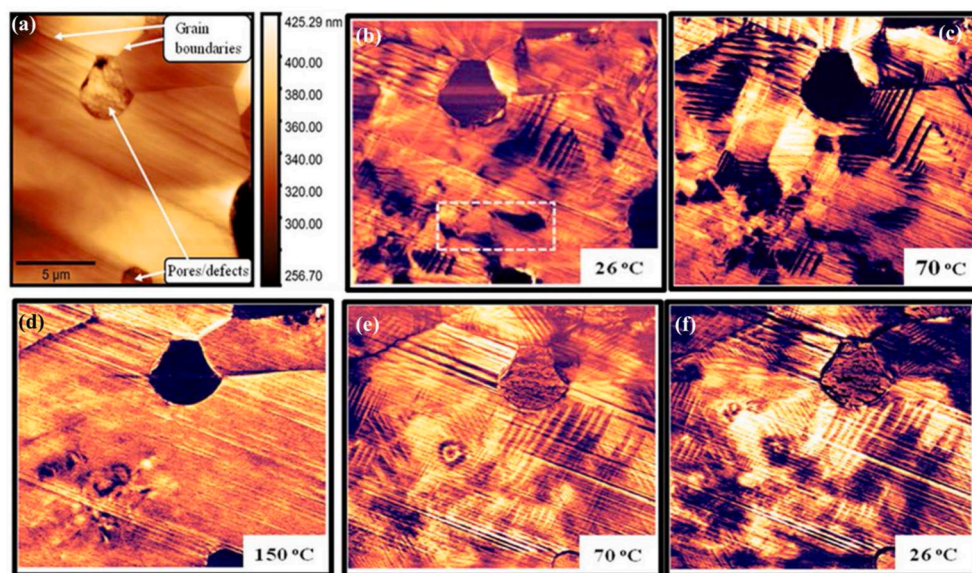


**Fig. 8.** (colour online) (a) Topography of the polished specimen of the BCZT ceramic Vertical piezoresponse force microscopy (VPFM) images at various temperatures. (b)–(d) represent images when heated from 26 °C to 150 °C while (e)–(f) show images while the sample was cooled.

When the temperature increases to 70 °C (Fig. 8c), the ceramic evolves to the tetragonal phase and is accompanied with an observable reorganization of domain structures between 26 °C and 70 °C. At 70 °C, there is increased stability of the tetragonal phase and the domain evolution is characterized by an increase in 90°-lamellar domains along with more distinct domain boundaries. Still further, as the temperature is increased to 150 °C (Fig. 8d), the lamellar domains fade away only to reappear when the sample was cooled to room temperature (Fig. 8f) through the tetragonal phase transition at 70 °C (Fig. 8e). The dissolution of the lamellar domains at high temperature signifies the transition to the paraelectric cubic phase. It is noteworthy that, even at 150 °C, there exist regions with blotched domain structure. Perseverance of the polar regions beyond  $T_c$  is in line with the observation of otherwise forbidden Raman modes in the cubic phase (as discussed in the preceding section IIIa on Raman spectroscopy).

2.5. Low-temperature dependence of photoluminescence

Fig. 9a illustrates the PL emission spectra measured at various temperatures between 20 and 150 K, observed under the excitation of a laser beam with a wavelength of 325 nm. The PL emission exhibits a broad band covering a large part of the visible spectra. Fig. 9b shows PL spectra

at a few selected temperatures, deconvoluted into four distinct bands or colour components showing their respective photon energy maxima (~2.55eV:blue, ~2.32eV:green, ~2.08eV:orange and ~1.78eV:red). The PL profile is typical of a multiphoton process involving different electronic transitions generated by different degrees of structural order-disorder in the studied ceramic [56]. It is also evident that, with increasing temperature, there is no appreciable frequency shift but PL intensity changes drastically. Since no dopant (i.e. a PL emission center) was intentionally added to BCZT, the observed emission is, therefore, due to the existence of intrinsic defects rather than to an extrinsic PL mechanism. It is well known that the electron band structure of ordered parent compound BTO has low-lying narrow conduction bands from Ti-3d orbitals and valence bands from O-2p states and the band gap,  $E_g$  ranges between 2.9 and 3.4 eV for the tetragonal phase; while  $E_g$  is higher (~4.9 eV) at lower temperatures in the rhombohedral phase [57]. From our PL results in BCZT performed in the R phase, it is quite apparent that the excitation energy 3.81 eV (325 nm) is lower than  $E_g$  and the maximum profile emission centered at ~2.55 eV is also lower than the band gap energy. Therefore, it is understood that certain localized luminescence states must exist within the band gap because the direct recombination of a conduction electron (in the Ti-3d and/or Zr-4d orbitals) and a hole in the O-2p valence band is unlikely.

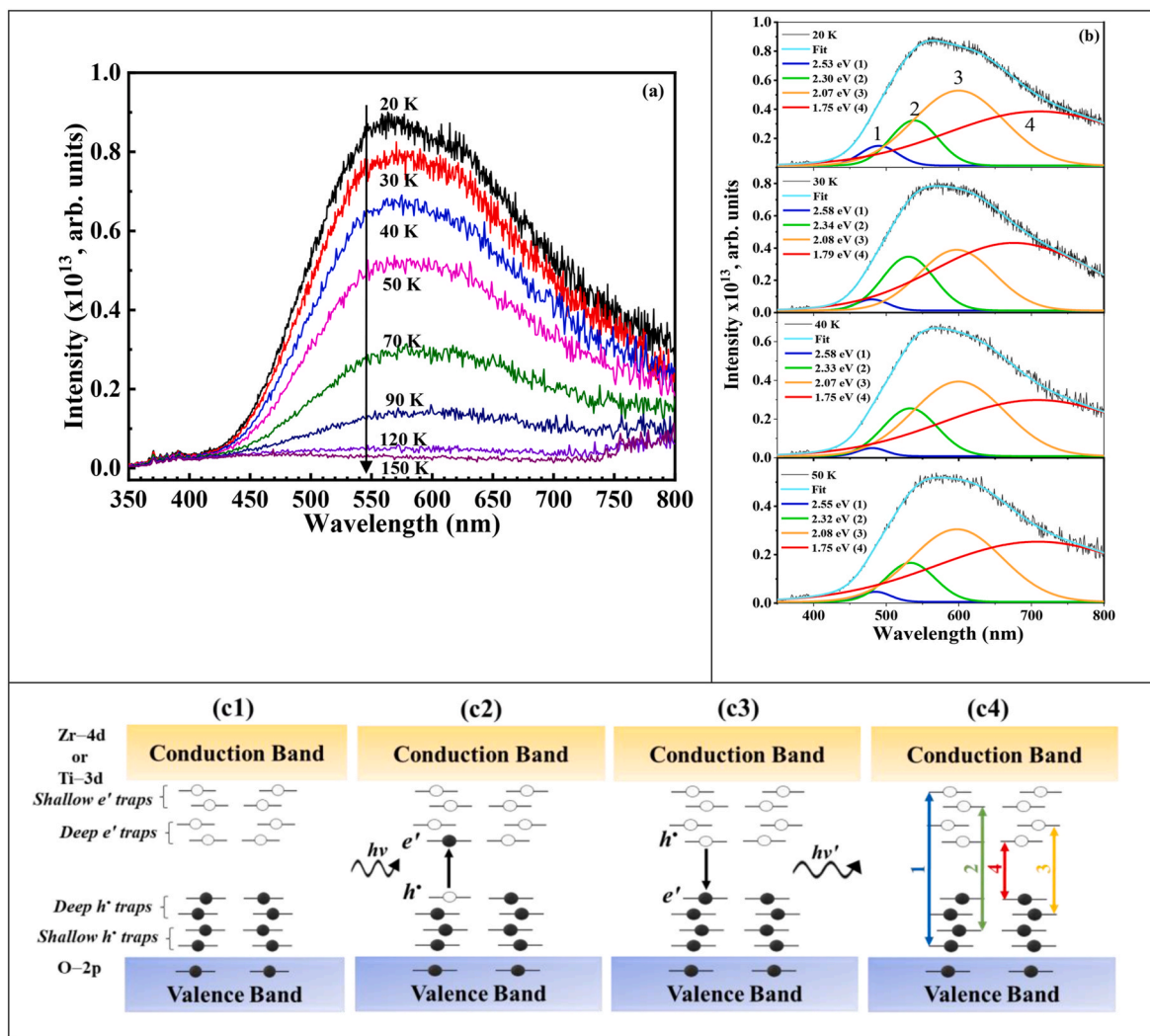


Fig. 9. (a) Evolution of photoluminescence spectra in BCZT with temperature from 20 K to 150 K, (b) Deconvolution of PL spectra into four colour components (1: Blue; 2:Green; 3:Orange and 4:Red) at selected temperatures, (c) Wide band model: (c1) before excitation (c2) excitation → formation of STE, and (c3) after excitation → recombination of  $e'$  and  $h^*$  for the PL emission (c4) transitions in shallow traps associated with visible colour centres 1,2 and deep traps with colour centres 3,4. (For interpretation of the references to colour in this figure legend, the reader is referred to the Web version of this article.)

The photoluminescent properties of titanates and zirconates with a disordered perovskite structure have been studied by several authors owing to the distinct potential of these materials for electro-optic applications [58–61]. The optical properties of such disordered structures are, in general, characterized by the presence of a broad PL band. It was proposed that the localized electronic states within the energy band gap act as radiative centres and account for the observed intense PL response. For instance, in their report on  $\text{Ba}(\text{Zr}_{0.25}\text{Ti}_{0.75})\text{O}_3$  thin films, Cavalcante et al. [62] put forth a theoretical model to account for the observed intense visible PL. They explained that the intermediate states were caused by structural defects such as  $[\text{ZrO}_5]\text{-}[\text{TiO}_6]$  or  $[\text{ZrO}_6]\text{-}[\text{TiO}_5]$  clusters and that the oxygen vacancies ( $V_{\text{O}}^{\bullet\bullet} = V_{\text{O}}^{\bullet}, V_{\text{O}}^{\bullet}, V_{\text{O}}^{\bullet\bullet}$ ) play an important role in the PL emission via recombination of electrons in oxygen vacancies with photoexcited holes. Fig. 9c1 illustrates the conduction band formed due to Zr-4d and or Ti-3d energy levels and the valence band created from O-2p levels. The shallow and deep trap levels, formed due to structural defects and oxygen vacancies in the band gap, are also shown. With the incidence of laser photon of energy  $h\nu$ , electrons are excited from the deep (shallow) hole traps to the deep (shallow) electron traps. The excited electron and the newly created hole form what is called a self-trapped exciton (STE) [63], as shown in Fig. 9c2. When the excited electron ( $e'$ ) jumps back to its original state, the electron recombines with the hole ( $h^*$ ) and the difference of energy ( $h\nu'$ ) is emitted as a photon (Fig. 9c3). Fig. 9c4 depicts the mechanism of the generation of four colours observed in Fig. 9b.

The temperature dependence of PL reveals that as the temperature rises, the PL intensity becomes rather weak (Fig. 9a) and quenching occurs at about 150 K in BCZT. This occurrence indicates a decrease in STEs and the ensuing low recombination rate [60]. Also, the peak PL wavelength did not show any shift with temperature. In general, a discontinuity in the variation of PL wavelength with temperature indicates a phase transition, which is not detected in this case indicating the absence of any phase transition in the studied temperature range.

### 3. Conclusions

High-quality  $(\text{Ba}_{0.85}\text{Ca}_{0.15})(\text{Zr}_{0.10}\text{Ti}_{0.90})\text{O}_3$  ceramic was fabricated by the solid-state reaction method. Rietveld refinement of the room temperature XRD data revealed that the composition is characterized by the coexistence of three phases: tetragonal ( $P4mm$ ), orthorhombic ( $Amm2$ ) and rhombohedral ( $R3m$ ), with tetragonal as a dominant phase. Detailed analysis of Raman spectroscopy results not only validated the existence of the intermediate orthorhombic phase but also signalled the presence of a subtle transition from  $R3c$  to  $R3m$  in the rhombohedral phase. The exhaustive investigation of temperature evolution of intensity, bandwidth, and frequency shift of Raman modes confirms the phase sequence as:  $R (R3c) \rightarrow R (R3m) \rightarrow O \rightarrow T \rightarrow C$  in the BCZT compound. It is also concluded that the  $R3m$  phase is preserved as a metastable phase in the  $Amm2$  stability region and the existence of both  $Amm2$  and  $R3m$  as metastable phases near room temperature is confirmed. All these observed changes may be understood as a result of the subtle balance of forces required to stabilize the intermediate tetragonal and orthorhombic phases in Ca- and Zr co-doped BTO and correspond to the modifications in the short-range order that occur upon rearrangement of the respective  $R$ ,  $O$ ,  $T$  and  $C$  phase fractions. The above results are indicative of the very sluggish nature of the transitions in the BCZT in general.

Besides, temperature-dependent local PFM studies showed apparent changes in the domain configurations implying a transition from co-existing phases at ambient temperature to a stable tetragonal, and finally to a cubic phase. Photoluminescence spectra showed four distinct bands or colour components with respective photon energy maxima ( $\sim 2.55\text{eV}$ :blue,  $\sim 2.32\text{eV}$ :green,  $\sim 2.08\text{eV}$ :orange and  $\sim 1.78\text{eV}$ :red). PL spectroscopy studies revealed that the addition of Ca and Zr into BTO not only causes structural disorder in the system but also indicated the existence of self-trapped excitons in the BCZT system.

### Declaration of competing interest

The authors declare that they have no known competing financial interests or personal relationships that could have appeared to influence the work reported in this paper

### Acknowledgements

I.C. would like to thank financial assistance by national funds (OE), through FCT – Fundação para a Ciência e a Tecnologia, I.P., in the scope of the framework contract foreseen in the numbers 4, 5 and 6 of the article 23, of the Decree-Law 57/2016, of August 29, changed by Law 57/2017, of July 19. This work was developed within the scope of the project CICECO-Aveiro Institute of Materials, UIDB/50011/2020 & UIDP/50011/2020, financed by national funds through the Portuguese Foundation for Science and Technology/MCTES. The authors would also like to acknowledge the Ural Center for Shared Use “Modern nanotechnology”, Ural Federal University, Russia and the Krasnoyarsk Regional Center of Research Equipment of Federal Research Center “Krasnoyarsk Science Center SB RAS”. The authors would like to thank Dr. E. Venkata Ramana, Department of Physics, University of Aveiro for the dielectric measurements. The work was supported by Government of the Russian Federation (Act 211, 440 Agreement 02.A03.21.0006).

### References

- [1] W.F. Liu, X.B. Ren, Large piezoelectric effect in Pb-free ceramics, *Phys. Rev. Lett.* 103 (2009) 257602.
- [2] A. Mondal, P. Saha, B. Ghosh, M. Sahu, G.D. Mukherjee, R. Ranjan, K. Brajesh, High-pressure structural investigation on lead-free piezoelectric 0.5Ba (Ti 0.8Zr0.2)O3 - 0.5(Ba0.7Ca0.3)TiO3, *J. Am. Ceram. Soc.* 103 (2020) 5259–5269.
- [3] Z. Hanani, S. Merselmiz, A. Danine, N. Stein, D. Mezzane, M. Amjoud, M. Lahcini, Y. Gagou, M. Spreitzer, D. Vengust, Z. Kutnjak, M.E. Marssi, I.A. Lukyanchuk, M. Gouné, Enhanced dielectric and electrocaloric properties in lead-free rod-like BCZT ceramics, *J. Adv. Ceram.* 9 (2020) 210.
- [4] X.W. Wang, B.H. Zhang, Y.C. Shi, Y.Y. Li, M. Manikandan, S.Y. Shang, J. Shang, Y. C. Hu, S.Q. Yin, Enhanced energy storage properties in  $\text{Ba}_{0.85}\text{Ca}_{0.15}\text{Zr}_{0.1}\text{Ti}_{0.9}\text{O}_3$  ceramics with glass additives, *J. Appl. Phys.* 127 (2020), 074103.
- [5] F. Fenga, Y. Yan, Large electrostrictive effect in Mn-doped BCZT ferroelectric ceramics, *Ceram. Int.* 45 (2019) 21315.
- [6] X. Chen, X. Chao, Z. Yang, Submicron barium calcium zirconium titanate ceramic for energy storage synthesised via the co-precipitation method, *Mater. Res. Bull.* 111 (2019) 259.
- [7] Y. Liu, Y. Chang, S. Yang, F. Li, Y. Sun, J. Wu, B. Yang, W. Cao, Improved densification behavior and energy harvesting properties of low-temperature sintered (Ba, Ca)(Zr, Ti)O<sub>3</sub> piezoceramics with a CuO additive, *Ceram. Int.* 45 (2019) 10518.
- [8] X. Xia, X. Jiang, C. Chen, X. Jiang, N. Tu, Y. Chen, Effects of Cr<sub>2</sub>O<sub>3</sub> doping on the microstructure and electrical properties of (Ba,Ca)(Zr,Ti)O<sub>3</sub> lead-free ceramics, *Front. Mater. Sci.* 10 (2016) 203.
- [9] M. Abdesslem, A. Aydi, N. Abdelmoula, Raman scattering, structural, electrical studies and conduction mechanism of  $\text{Ba}_{0.9}\text{Ca}_{0.1}\text{Ti}_{0.95}\text{Zr}_{0.05}\text{O}_3$  ceramic, *J. Alloys Compd.* 774 (2019) 685.
- [10] H. Kaddoussi, A. Lahmar, Y. Gagou, B. Manoun, J.N. Chotard, J.-L. Dellis, Z. Kutnjak, H. Khemakhem, B. Elouadi, M. El Marssi, Sequence of structural transitions and electrocaloric properties in  $(\text{Ba}_{1-x}\text{Ca}_x)(\text{Zr}_{0.1}\text{Ti}_{0.9})\text{O}_3$  ceramics, *J. Alloys Compd.* 713 (2017) 164.
- [11a] D. Damjanovic, A. Biancoli, L. Batooli, A. Vahabzadeh, J. Trodahl, Elastic, dielectric, and piezoelectric anomalies and Raman spectroscopy of 0.5Ba (Ti0.8Zr0.2)O3-0.5(Ba0.7Ca0.3)TiO3, *Appl. Phys. Lett.* 100 (2012) 192907.
- [11b] L. Zhang, M. Zhang, L. Wang, C. Zhou, Z. Zhang, Y. Yao, L. Zhang, D. Xue, X. Lou, X. Ren, Phase transitions and the piezoelectricity around morphotropic phase boundary in  $\text{Ba}(\text{Zr}_{0.2}\text{Ti}_{0.8})\text{O}_3\text{-x}(\text{Ba}_{0.7}\text{Ca}_{0.3})\text{TiO}_3$  lead-free solid solution, *Appl. Phys. Lett.* 105 (2014) 162908.
- [12] P.S. Dabal, A. Dixit, R.S. Katiyar, D. Garcia, R. Guo, A.S. Bhalla, Micro-Raman study of  $\text{Ba}_{1-x}\text{Sr}_x\text{TiO}_3$  ceramics, *J. Raman Spectrosc.* 32 (2001) 147.
- [13] P.S. Dabal, R.S. Katiyar, Studies on ferroelectric perovskites and Bi-layered compounds using micro-Raman spectroscopy, *J. Raman Spectrosc.* 33 (2002) 405.
- [14] C. Ma, W. Zhou, Z. Gan, X. Wang, W. Tan, Z. Zhang, Z. Zhai, Upconversion photoluminescence modulation by electric field poling in  $\text{Er}^{3+}$  doped  $(\text{Ba}_{0.85}\text{Ca}_{0.15})(\text{Zr}_{0.1}\text{Ti}_{0.9})\text{O}_3$  piezoelectric ceramics, *J. Alloys Compd.* 794 (2019) 325.
- [15] Z. Wang, W. Li, R. Chu, J. Hao, Z. Xu, G. Li, Strong luminescence and high piezoelectric properties in Pr-doped  $(\text{Ba}_{0.99}\text{Ca}_{0.01})(\text{Ti}_{0.98}\text{Zr}_{0.02})\text{O}_3$  multifunctional ceramics, *J. Alloys Compd.* 689 (2016) 30.
- [16] C. Ma, X. Wang, Z. Gan, W. Tan, X. Wang, J. Zhang, W. Zhou, Photoluminescence and optical temperature sensing in  $\text{Sm}^{3+}$ -doped  $\text{Ba}_{0.85}\text{Ca}_{0.15}\text{Ti}_{0.90}\text{Zr}_{0.10}\text{O}_3$  lead-free ceramics, *Ceram. Int.* 45 (2019) 588.

- [17] Y. Tian, X. Chao, L. Jin, L. Wei, P. Liang, Z. Yang, Polymorphic structure evolution and large piezoelectric response of lead-free (Ba,Ca)(Zr,Ti)O<sub>3</sub> ceramics, *Appl. Phys. Lett.* 104 (2014) 112901.
- [18] K. Brajesh, M. Abebe, R. Ranjan, Structural transformations in morphotropic-phase-boundary composition of the lead-free piezoelectric system Ba(Ti<sub>0.8</sub>Zr<sub>0.2</sub>)O<sub>3</sub>–(Ba<sub>0.7</sub>Ca<sub>0.3</sub>)TiO<sub>3</sub>, *Phys. Rev. B* 94 (2016) 104108.
- [19] A.C. Larson, R.B. Von Dreele, "General Structure Analysis System (GSAS)", Los Alamos National Laboratory Report LAUR 86, 2000, p. 748.
- [20] B.H. Toby, EXPGUI, a graphical user interface for GSAS, *J. Appl. Crystallogr.* 34 (2001) 210.
- [21] U.D. Venkateswaran, V.M. Naik, R. Naik, High-pressure Raman studies of polycrystalline BaTiO<sub>3</sub>, *Phys. Rev. B* 58 (1998) 14256.
- [22] J.D. Freire, R.S. Katiyar, Lattice dynamics of crystals with tetragonal BaTiO<sub>3</sub> structure, *Phys. Rev. B* 37 (1988) 2074.
- [23] M. DiDomenico, S.H. Wemple, S.P.S. Porto, Raman Spectrum of single-domain BaTiO<sub>3</sub>, *Phys. Rev.* 174 (1968) 522.
- [24] Q. Zhang, J. Zhai, L. Kong, X. Yao, Investigation of ferroelectric phase transition for barium strontium titanate ceramics by in situ Raman scattering, *J. Appl. Phys.* 112 (2012) 124112.
- [25] D.-Y. Lu, W. Cheng, X.-Y. Sun, Q.-L. Liu, D.-X. Lib, Z.-Y. Li, Abnormal Raman spectra in Er-doped BaTiO<sub>3</sub> ceramics, *J. Raman Spectrosc.* 45 (2014) 963.
- [26] F.M. Pontes, M.T. Escote, C.C. Escudeiro, E.R. Leite, E. Longo, A.J. Chiquito, P. S. Pizani, J.A. Varela, Characterization of BaTi<sub>1-x</sub>Zr<sub>x</sub>O<sub>3</sub> thin films obtained by a soft chemical spin-coating technique, *J. Appl. Phys.* 96 (2004) 4386.
- [27] T. Hoshina, H. Kakemoto, T. Tsurumi, S. Wada, M. Yashima, Size and temperature induced phase transition behaviors of barium titanate nanoparticles, *J. Appl. Phys.* 99 (2006), 054311.
- [28] V. Buscaglia, M.T. Buscaglia, M. Viviani, L. Mitoseriu, P. Nanni, V. Trefiletti, P. Piaggio, I. Gregora, T. Ostapchuk, J. Pokorný, J. Petzelt, Grain size and grain boundary-related effects on the properties of nanocrystalline barium titanate ceramics, *J. Eur. Ceram. Soc.* 26 (2006) 2889.
- [29] R. Farhi, M. El Marssi, A. Simon, J. Ravez, A Raman and dielectric study of ferroelectric ceramics, *Eur. Phys. J.*, B 9 (1999) 599.
- [30] P.S. Dobal, A. Dixit, R.S. Katiyar, Z. Yu, R. Guo, A.S. Bhalla, Phase transition behavior of BaZr<sub>x</sub>Ti<sub>1-x</sub>O<sub>3</sub> ceramics, *J. Raman Spectrosc.* 32 (2001) 69.
- [31] A. Feteira, R. Elsebrock, A. Dias, R.L. Moreira, M.T. Lanagan, D.C. Sinclair, Synthesis and characterisation of La<sub>0.4</sub>Ba<sub>0.6</sub>Ti<sub>0.6</sub>RE<sub>0.4</sub>O<sub>3</sub> (where RE = Y, Yb) ceramics, *J. Eur. Ceram. Soc.* 26 (2006) 1947.
- [32] Z.Ž. Lazarević, M.M. Vijatović, B.D. Stojanović, M.J. Romčević, N.Ž. Romčević, Structure study of nanosized La- and Sb-doped BaTiO<sub>3</sub>, *J. Alloys Compd.* 494 (2010) 472.
- [33] J. Kreisel, P. Bouvier, M. Maglione, B. Dkhil, A. Simon, High-pressure Raman investigation of the Pb-free relaxor BaTi<sub>0.65</sub>Zr<sub>0.35</sub>O<sub>3</sub>, *Phys. Rev. B* 69 (2004), 092104.
- [34] S. Miao, J. Pokorný, U.M. Pasha, O.P. Thakur, D.C. Sinclair, I.M. Reaney, Polar order and diffuse scatter in Ba(Ti<sub>1-x</sub>Zr<sub>x</sub>)O<sub>3</sub> ceramics, *J. Appl. Phys.* 106 (2009) 114111.
- [35] M. Deluca, C.A. Vasilescu, A.C. Ianculescu, D.C. Berger, C.E. Ciomaga, L. P. Curecheriu, L. Stoleriu, A. Gajović, L. Mitoseriu, C. Galassi, Investigation of the composition-dependent properties of BaTi<sub>1-x</sub>Zr<sub>x</sub>O<sub>3</sub> ceramics prepared by the modified Pechini method, *J. Eur. Ceram. Soc.* 32 (2012) 3551.
- [36] W. Janbua, T. Bongkarn, T. Kolodiazny, N. Vittayakorn, High piezoelectric response and polymorphic phase region in the lead-free piezoelectric BaTiO<sub>3</sub>–CaTiO<sub>3</sub>–BaSnO<sub>3</sub> ternary system, *RSC Adv.* 7 (2017) 30166.
- [37] M. Deluca, L. Stoleriu, L.P. Curecheriu, N. Horchidan, A.C. Ianculescu, C. Galassi, L. Mitoseriu, High-field dielectric properties and Raman spectroscopic investigation of the ferroelectric-to-relaxor crossover in BaSn<sub>x</sub>Ti<sub>1-x</sub>O<sub>3</sub> ceramics, *J. Appl. Phys.* 111 (2012), 084102.
- [38] V. Buscaglia, S. Tripathi, V. Petkov, M. Dapiaggi, M. Deluca, A. Gajović, Y. Ren, Average and local atomic-scale structure in BaZr<sub>x</sub>Ti<sub>1-x</sub>O<sub>3</sub> (x = 0.10, 0.20, 0.40) ceramics by high-energy x-ray diffraction and Raman spectroscopy, *J. Phys. Condens. Matter* 26 (2014), 065901.
- [39] E. Buixaderas, D. Nuzhnyy, J. Petzelt, Li Jin, D. Damjanovic, Polar lattice vibrations and phase transition dynamics in Pb(Zr<sub>1-x</sub>Ti<sub>x</sub>)O<sub>3</sub>, *Phys. Rev. B* 84 (2011) 184302.
- [40] J. Frantti, Y. Fujioka, A. Puretzy, Y. Xie, Z.-G. Ye, C. Parish, A.M. Glazer, Phase transitions and thermal-stress-induced structural changes in a ferroelectric Pb(Zr<sub>0.80</sub>Ti<sub>0.20</sub>)O<sub>3</sub> single crystal, *J. Phys. Condens. Matter* 27 (2015), 025901.
- [41] F. Cordero, E. Buixaderas, C. Galassi, Damage from coexistence of ferroelectric and antiferroelectric domains and clustering of O vacancies in PZT: an elastic and Raman study, *Materials* 12 (2019) 957.
- [42] D.I. Woodward, J. Knudsen, I.M. Reaney, Review of crystal and domain structures in the PbZr<sub>x</sub>Ti<sub>1-x</sub>O<sub>3</sub> solid solution, *Phys. Rev. B* 72 (2005) 104110.
- [43] E. Buixaderas, I. Gregora, S. Kamba, J. Petzelt, M. Kosec, Raman spectroscopy and effective dielectric function in PLZT x/40/60, *J. Phys. Condens. Matter* 20 (2008) 345229.
- [44] L. Zhao, B.-P. Zhang, P.-F. Zhou, X.-K. Zhao, L.-F. Zhu, Phase Structure and property Evaluation of (Ba,Ca)(Ti,Sn)O<sub>3</sub> Sintered with Li<sub>2</sub>CO<sub>3</sub> Addition at low temperature, *J. Am. Ceram. Soc.* 97 (2014) 2164.
- [45] Y.-J. Jiang, L.-Z. Zeng, R.-P. Wang, Y. Zhu, Y.-L. Liu, Fundamental and second-order Raman Spectra of BaTiO<sub>3</sub>, *J. Raman Spectrosc.* 27 (1996) 31.
- [46] J.F. Scott, Soft-mode spectroscopy: experimental studies of structural phase transitions, *Rev. Mod. Phys.* 46 (1974) 83.
- [47] M.P. Fontana, M. Lambert, Linear disorder and temperature dependence of Raman scattering in BaTiO<sub>3</sub>, *Solid State Commun.* 10 (1972) 1.
- [48] U. Bianchi, W. Kleemann, J.G. Bednorz, Raman scattering of ferroelectric Sr 1-xCaxTiO<sub>3</sub>, x = 0.007, *J. Phys. Condens. Matter* 6 (1994) 1229.
- [49] W. Hayes, R. Loudon, *Scattering of Light by Crystals*, Wiley & Sons, New York, NY, 1978.
- [50] H. Taniguchi, M. Itoha, D. Fu, Raman scattering study of the soft mode in Pb(Mg<sub>1/3</sub>Nb<sub>2/3</sub>)O<sub>3</sub>, *J. Raman Spectrosc.* 42 (2011) 706.
- [51] T.P. Dougherty, G.P. Wiederrecht, K.A. Nelson, M.H. Garrett, H.P. Jenson, C. Warde, Femtosecond time-resolved spectroscopy of soft modes in structural phase transitions of perovskites, *Phys. Rev. B* 50 (1994) 8996.
- [52] B. Chaabane, J. Kreisel, P. Bouvier, G. Lucazeau, B. Dkhil, Effect of high pressure on the Pb(Mg<sub>1/3</sub>Nb<sub>2/3</sub>)O<sub>3</sub>–PbTiO<sub>3</sub> solid solution: a Raman scattering investigation, *Phys. Rev. B* 70 (2004) 134114.
- [53] J. Kreisel, B. Dkhil, P. Bouvier, J.M. Kiat, Effect of high pressure on relaxor ferroelectrics, *Phys. Rev. B* 65 (2002) 172101.
- [54] M. Deluca, L. Stoleriu, L.P. Curecheriu, N. Horchidan, A. Carmen Ianculescu, C. Galassi, L. Mitoseriu, High-field dielectric properties and Raman spectroscopic investigation of the ferroelectric-to-relaxor crossover in BaSn<sub>x</sub>Ti<sub>1-x</sub>O<sub>3</sub> ceramics, *J. Appl. Phys.* 111 (2012), 084102.
- [55] J. Gao, D. Xue, Y. Wang, D. Wang, L. Zhang, H. Wu, S. Guo, H. Bao, C. Zhou, W. Liu, S. Hou, G. Xiao, X. Ren, Microstructure basis for strong piezoelectricity in Pb-free Ba(Zr<sub>0.2</sub>Ti<sub>0.8</sub>)O<sub>3</sub>–(Ba<sub>0.7</sub>Ca<sub>0.3</sub>)TiO<sub>3</sub> ceramics, *Appl. Phys. Lett.* 99 (2011), 092901.
- [56] V.M. Longo, L.S. Cavalcante, A.T. de Figueiredo, L.P.S. Santos, E. Longo, J. A. Varela, J.R. Sambrano, C.A. Parkocimas, F.S. De Vicente, A.C. Hernades, Highly intense violet-blue light emission at room temperature in structurally disordered SrZrO<sub>3</sub> powders, *Appl. Phys. Lett.* 90 (2007), 091906.
- [57a] A. Mahmoud, A. Erba, K.E. El-Kelany, M. Rérat, R. Orlando, Low-temperature phase of BaTiO<sub>3</sub>: piezoelectric, dielectric, elastic, and photoelastic properties from ab initio simulations, *Phys. Rev. B* 89 (2014), 045103.
- [57b] R.A. Evarestov, A. Bandura, First-principles calculations on the four phases of BaTiO<sub>3</sub>, *J. Comp. Chem.* 33 (2012) 1123.
- [58] P.S. Pizani, H.C. Basso, F. Lanciotti, T.M. Baschi, F.M. Pontes, E. Longo, E.R. Leite, Visible photoluminescence in amorphous ABO<sub>3</sub> perovskites, *Appl. Phys. Lett.* 81 (2002) 253.
- [59] M. Aguilar, F. Agullo-Lopez, X-ray induced processes in SrTiO<sub>3</sub>, *J. Appl. Phys.* 53 (1982) 9009.
- [60] S.G. Lu, Z.K. Xu, H. Chen, C.L. Mak, K.H. Wong, K.F. Li, K.W. Cheah, Time-resolved photoluminescence of barium titanate ultrafine powders, *J. Appl. Phys.* 99 (2006), 064103.
- [61] M.L. Moreira, M.F.C. Gurgel, G.P. Mambrini, E.R. Leite, P.S. Pizani, J.A. Varela, E. Longo, Photoluminescence of barium titanate and barium zirconate in multilayer disordered thin films at room temperature, *J. Phys. Chem.* 112 (2008) 8938.
- [62] L.S. Cavalcante, M.F.C. Gurgel, A.Z. Simões, E. Longo, J.A. Varela, M.R. Joya, P. S. Pizani, Intense visible photoluminescence in Ba(Zr<sub>0.25</sub>Ti<sub>0.75</sub>)O<sub>3</sub> thin films, *Appl. Phys. Lett.* 90 (2007), 011901.
- [63] K.S. Song, R.T. Williams, Self-trapped excitons, in: *Springer Series in Solid-State Sciences*, vol. 105, Springer-Verlag, Berlin, 1993.